Opto-Electronic Advances

Supplementary information

May 2025, Vol. 8, No. 5

DOI: 10.29026/oea.2025.240250 CSTR: 32247.14.oea.2025.240250

Terahertz active multi-channel vortices with parity symmetry breaking and near/far field multiplexing based on a dielectric-liquid crystal-plasmonic metadevice

Yiming Wang[1], Fei Fan[1,2]*, Huijun Zhao[1], Yunyun Ji[2], Jing Liu[1] and Shengjiang Chang[2]

[1]Institute of Modern Optics, Nankai University, Tianjin Key Laboratory of Micro-scale Optical Information Science and Technology, Tianjin 300350, China; [2]Tianjin Key Laboratory of Optoelectronic Sensor and Sensing Network Technology, Tianjin 300350, China.
*Correspondence: F Fan, E-mail: fanfei@nankai.edu.cn

This file includes:

Supplementary information for this paper is available at https://doi.org/10.29026/oea.2025.240250

Section 1. Design of plasmonic metasurface layer

The schematic diagram of the metal slit on the plasmonic metasurface is displayed in Fig. 2(a) of the main text. To evaluate the proportion of the circular-to-linear polarization conversion, the degree of LP is defined as $D_{\mathrm{LP}} = \sqrt{s_1^2 + s_2^2}/s_0$, which is related to the slit dimensions, where $s_0 - s_2$ are stokes parameters. Fig S1(a) shows the D_{LP} as a function of the slit geometric sizes (a and b) at the frequency f_0 = 0.475 THz, that is $D_{\mathrm{LP}} \approx 1$ corresponding to the geometry of 160 μm×50 μm. And Fig. 2(a) shows this y-oriented slit array performs well to x-polarized transmission at the central frequency f_0 = 0.475 THz, reaching a high transmission of nearly 90% in simulation and over 70% experimentally. These results indicates a significant SPW launching has been achieved.

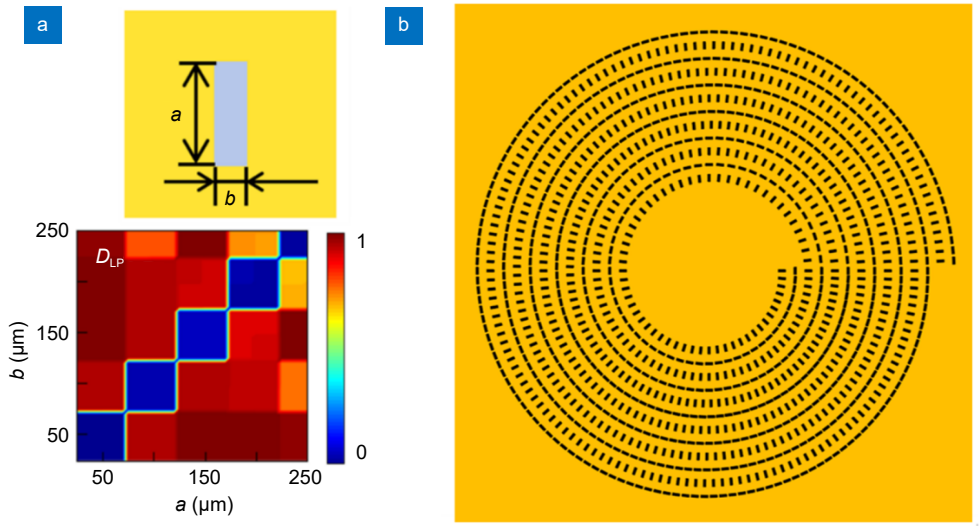

Fig. S1 | (**a**) The D_{LP} results as a function of the slit geometric sizes (a and b) at the frequency f_0 = 0.475 THz. (**b**) An enlarged diagram of the plasmonic metasurface structure.

The schematic diagram of the plasmonic metasurface is displayed in Fig. S1(b), which consists of six ring archimedean spiral-arrayed pair slit resonators (ASPS) (k = 1–6). Each ring resonator is composed of m slit-pairs arranged at uniform angular spacing, with their orientation angle $\varphi_{m,\mathrm{k}}$ equal to the azimuth angle φ_{M}. The center position M of m^{th} slit-pair is set as follows:

$$r_{m,k} = R_{0,k} - \lambda_{\mathrm{SP}}\varphi_{m,k} \Big/ 2\pi \,, \tag{S1}$$

$$\Delta R_{0,k} = \lambda_{\mathrm{SP}} \,, \tag{S2}$$

where $r_{m,\mathrm{k}}$ is the radius of the m^{th} slit-pair ($r_{\mathrm{m}} >> d/2$), $R_{0,k}$ is the initial radius corresponding to azimuth angle $\varphi_0 = 0$. As the radius variation increases from 0 to λ_{SP}, (λ_{SP} is the SP wavelength) the total propagation phase gradient of -2π is generated along the azimuthal direction. The setting ΔR_0 makes sure that SPWs excited from every ring meet the phase matching condition of constructive interference.

Moreover, in a certain slit-pair, these two slits are arranged with perpendicular orientation angles to each other and the distance between their geometric centers of $\lambda_{\mathrm{SP}}/2$, which can be described by the following formula:

$$\theta_{1,m} = \varphi_m + \pi/2 \,, \tag{S3}$$

$$\theta_{2,m} = \varphi_m \,, \tag{S4}$$

$$d = \lambda_{\mathrm{SP}}/2 \,, \tag{S5}$$

in which, $\theta_{1,m}$ and $\theta_{2,m}$ represent the orientation of the inner and outer slit of the m-th slit-pair, respectively; φ_m is the azimuthal angle of the m-th slit-pair to the x-axis. At this point, the total geometric phase of excited SPWs can be tuned

in the whole range of [0, 2πσ] under the CP incidence. The specific structural parameters of the plasmonic metasurface can be found in Table S1.

Table S1 | Geometric parameters of the ASPS.

k	λ_{SP} (μm)	$R_{0,\,k}$ (μm)	m_k
1	600	2400	60
2		3000	80
3		3600	105
4		4200	120
5		4800	135
6		5400	150

Under the spin photon incidence of E_{in} = (1, σi), the near-field distribution of plasmonic vortex at the center point O is the superposition of the surface wave fields from the slit pairs of ASPS can be expressed as[S1]:

$$E_{o,NF} = \frac{C}{\sqrt{\lambda_{sp} r_m}} e^{ik_{sp} r_m} e^{i\sigma(\theta_{2,m}+\theta_{1,m}-\varphi_M-\pi/2)} \sin(\theta_{2,m}-\theta_{1,m}) , \tag{S6}$$

wherein, C is a complex coefficient describing the SP excitation response of slit pairs. With the definition of$\theta_{1,m}$, $\theta_{2,m}$ and R_m in Eqs. (S1 – S5) of the manuscript, Eq. (S6) can be simplified to:

$$E_{o,NF} = \frac{C}{\sqrt{\lambda_{sp} r_m}} e^{ik_{sp} R_0} e^{i(\sigma-1)\varphi_M} . \tag{S7}$$

The far-field distribution contains both an incident spin-locked component without a phase shift and a spin-flipped component with a phase shift at twice the rotation angle known as the Pancheratnam-Berry geometric phase, of which the transmission matrix can be obtained as follows:

$$\begin{bmatrix} E_{M,Lout} \\ E_{M,Rout} \end{bmatrix} = \begin{bmatrix} t_{co,1} & t_{cro,1} e^{-i2\varphi_M} \\ t_{cro,1} e^{i2\varphi_M} & t_{co,1} \end{bmatrix} \begin{bmatrix} E_{M,Lin} \\ E_{M,Rin} \end{bmatrix}, (n=1) , \tag{S8}$$

$$\begin{bmatrix} E_{M,Lout} \\ E_{M,Rout} \end{bmatrix} = \begin{bmatrix} t_{co,2} & t_{cro,2} e^{-i2(\varphi_M+\pi/2)} \\ t_{cro,2} e^{i2(\varphi_M+\pi/2)} & t_{co,2} \end{bmatrix} \begin{bmatrix} E_{M,Lin} \\ E_{M,Rin} \end{bmatrix} = \begin{bmatrix} t_{co,2} & -t_{cro,2} e^{-i2\varphi_M} \\ -t_{cro,2} e^{i2\varphi_M} & t_{co,2} \end{bmatrix} \begin{bmatrix} E_{M,Lin} \\ E_{M,Rin} \end{bmatrix}, (n=2) , \tag{S9}$$

where t_{co} and t_{cro} are transmission coefficients of spin-locked components and the spin-flipped components under CP incidence, respectively. They are determined by the SP coupling efficiency related to the geometric sizes and different orientations of slits on the inner (n=1) and outer (n=2) sides in the slit pairs. Thus, the total FF transmitting process can be expressed as follows:

$$\begin{bmatrix} E_{M,Lout} \\ E_{M,Rout} \end{bmatrix} = \begin{bmatrix} t_{co,1}+t_{co,2} & (t_{cro,1}-t_{cro,2}) e^{-i2\varphi_M} \\ (t_{cro,1}-t_{cro,2}) e^{i2\varphi_M} & t_{co,1}+t_{co,2} \end{bmatrix} \begin{bmatrix} E_{M,Lin} \\ E_{M,Rin} \end{bmatrix} = \begin{bmatrix} t_{co} & t_{cro} e^{-i2\varphi_M} \\ t_{cro} e^{i2\varphi_M} & t_{co} \end{bmatrix} \begin{bmatrix} E_{M,Lin} \\ E_{M,Rin} \end{bmatrix} . \tag{S10}$$

Section 2. Design of dielectric metasurface layer

The dielectric metasurface is designed for u=3 and v=2 at the central frequency f_0. In this case, $\beta = \frac{1}{4}\varphi_{\mathrm{D}}$, $\Phi_x = \frac{5}{2}\varphi_{\mathrm{D}}$, $\Delta\Phi_{xy} = \pi$. Note that if the atom with the geometry of $q \times w$ leads to a phase shift of Φ_{x}, the atom with the geometry of $w \times q$ leads to a phase shift of $\Phi_{\mathrm{x}} - \pi$. Besides, the transmission of all atoms should be kept high to ensure the efficient generation of FVs, as shown in Fig. 3(b–d) of the main text. Thus, a series of pillars are selected to act as an HWP and cover a phase shift of $[-\pi, \pi]$.

Table S2 | Geometric parameters of dielectric meta-atoms.

Label	q (*μm*)	w (*μm*)	$\lvert\Phi_x\rvert$ (π)
1	95	167	0.92
2	262	111	0.72
3	75	170	0.49
4	200	105	0.24
5	185	102	0.05

Section 3. Discussion for transmission efficiency and mode purity

The transmission efficiency to the FF refers to the ratio of the total output energy to the input one, which can be described as follows:

$$T_{\mathrm{FF}} = I_{\mathrm{FF}} / I_{\mathrm{in}} = \frac{\iint_S |\boldsymbol{E}_{\mathrm{out}}(x,y)|^2 \mathrm{d}S}{\iint_S |\boldsymbol{E}_{\mathrm{in}}(x,y)|^2 \mathrm{d}S} . \tag{S11}$$

Besides, the near field efficiency describes the energy for SPW excitation (i.e. the longitudinal field component E_{z}), which can be calculated as follows:

$$T_{\mathrm{NF}} = I_{\mathrm{SPW}} / I_{\mathrm{in}} = \frac{\iint_S |E_z(x,y)|^2 \mathrm{d}S}{\iint_S |E_{in}(x,y)|^2 \mathrm{d}S} . \tag{S12}$$

The calculations of output and input energy are the integrals of the field intensity distribution on the effective x-y plane of the metasurface.

For the single plasmonic metasurface in the simulation, as shown in Fig. S2(a), the FF transmission efficiency is 58.7% for LCP excitation and 62.3% for RCP excitation. The NF efficiency of SPWs reaches 48.8% and 52.1%, respectively. Besides, for the single dielectric metasurface, the simulated FF efficiency shown in Fig. S2(b) reaches 55.7% and 57.4% corresponding to the LCP and RCP incidence. Moreover, it can be seen from Fig. S2(c) that the cascaded metadevice realizes the maximum efficiency of 54.1% for FF and 37.1% for NF.

The transmission efficiency has also been obtained by FF detection experimentally, 48% in the single plasmonic metasurface and 35% in the cascaded metadevice. However, the NF intensity is strongly related to the distance from the probe antenna to the metallic surface. Due to the lack of a standard reference of SPWs in experiments, the experimental transmission efficiency for NF is not provided here.

Besides, the mode purity results of the metasurfaces are supplementarily provided in Fig. S3, which is calculated by $\eta(\%) = I_t / \sum_S I_l$ shown in Eq. (7) in the main text. In simulation, the single dielectric metasurface excites the spin-decoupled FVs of (P=RL, l=3) and (P=LR, l=2) with high purity of 90.2% and 88.9%, respectively. For the single helical plasmonic metasurface, PVs are excited with 2 modes of (P=zL, l=0) and (P=zR, l=−2) with the purity of 94.4% and 90.5%, respectively in the NF channels, while FVs are excited with 4 modes of (P=LL, l=0), (P=RL, l=2), (P=LR, l=−2) and (P=RR, l=0) with the purity of 97.6%, 89.0%, 87.8% and 97.8%, respectively. In experiments, the mode purity of the dielectric metasurface is nearly 60%. The measured PV and FV mode purity of the plasmonic metasurface reaches over 60% and 55%, respectively. These results verify the good performance of these two metasurface layers in the vortex excitation with high efficiency and purity.

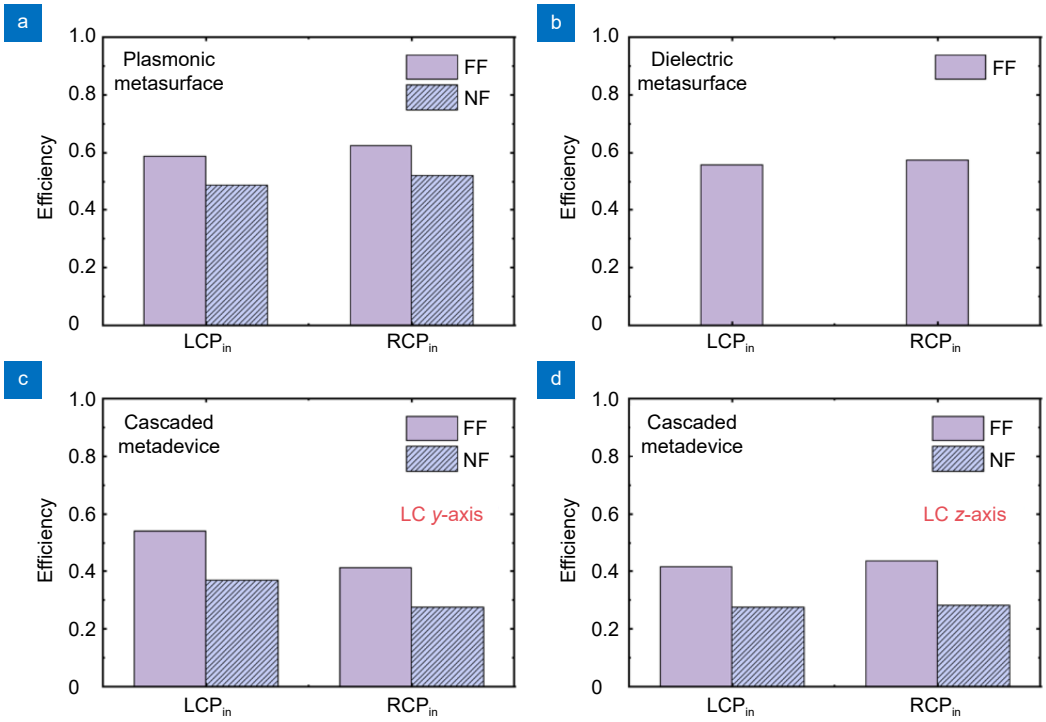

Fig. S2 | Simulated transmission efficiency of the (**a**) plasmonic metasurface, (**b**) dielectric metasurface, and (**c**) the designed cascaded metadevice when LC molecules oriented along *y*-axis and (**d**) *z*-axis.

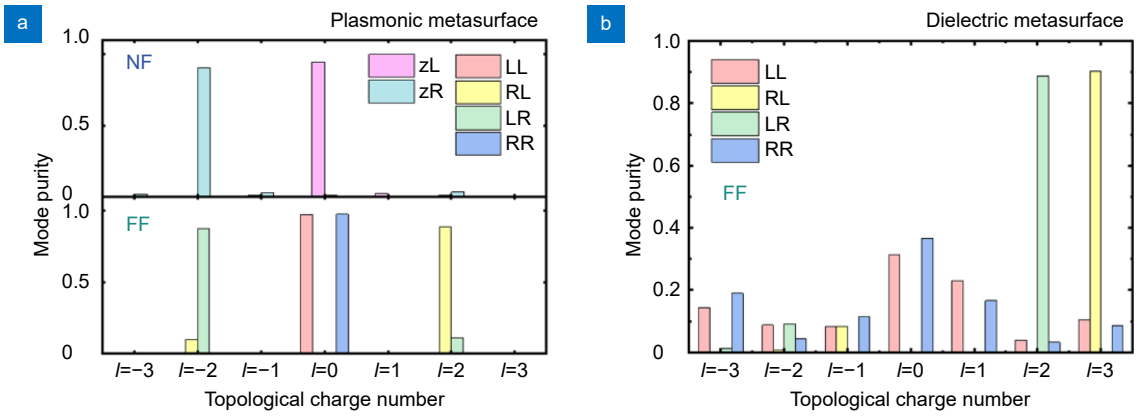

Fig. S3 | Simulated vortex mode purity in the single (**a**) plasmonic metasurface, and (**b**) dielectric metasurface.

Furthermore, for the cascaded metadevice, the experimental purity values of the vortex modes in each NF/FF channel at the different biases are shown in Fig. S4. With the bias turning from 0 V/mm to 35 V/mm, the mode purity of the 2 specific vortices corresponding to each channel is reversed, which indicates the active modulation in all 6 channels. The maximum modulation ratio for PVs and FVs reaches up to 88% and 86%, with the average measured purity of nearly 60% and 45%, respectively.

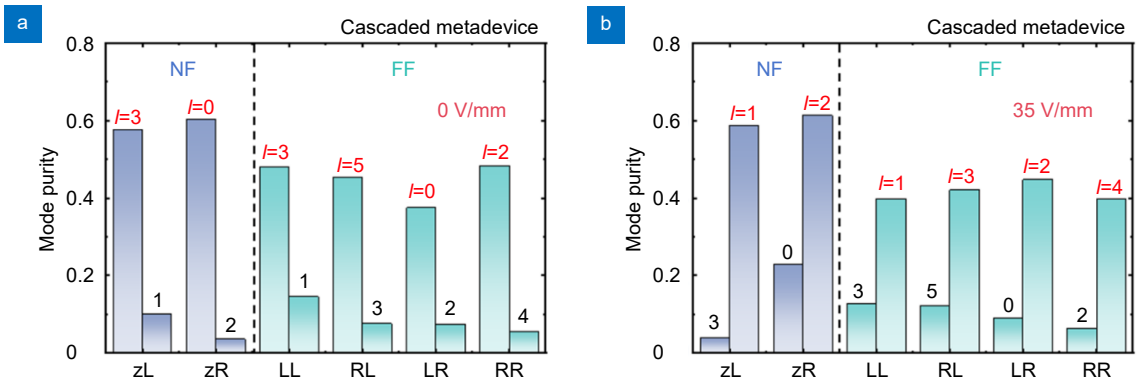

Fig. S4 | Experimental purity of the PV and FV modes in each channel of the cascaded metadevice, when applying the bias of (**a**) 0 V/mm and (**b**) 35 V/mm.

Section 4. Experimental data processing

For the NF detection, the used microprobe is the longitudinal probe for E_z. To obtain the arbitrary spin state of the input waves, by rotating the first THz polarizer to ±45°, the transmitted amplitude A and phase δ of these orthogonal signals can be obtained by Fourier transform. Thus the transmission of the PV modes with polarization state of zL and zR is given by:

$$\begin{bmatrix} E_{zL} \\ E_{zR} \end{bmatrix} = \frac{1}{\sqrt{2}} \begin{bmatrix} 1 & -\mathrm{i} \\ 1 & \mathrm{i} \end{bmatrix} \begin{bmatrix} A_+ \mathrm{e}^{\mathrm{i}\delta_+} \\ A_- \mathrm{e}^{\mathrm{i}\delta_-} \end{bmatrix}, \tag{S13}$$

where + and − are orthogonal LP components oriented in +45° and −45° directions, respectively.

To fully investigate the FF response, the entire polarization states of the FVs should be obtained, including the 2 co-polarization states (LL and RR) and 2 cross-polarization states (LR and RL). The first and the latter subscript represents the polarization state of the output and input component, respectively. To obtain these four spin states, by rotating the two THz polarizers to ±45° respectively, the four spin-locked and spin-flipped transmission coefficients can be measured as follows:

$$\begin{bmatrix} t_{rr} & t_{rl} \\ t_{lr} & t_{ll} \end{bmatrix} = \frac{1}{2} \begin{bmatrix} (t_{++} + t_{--}) + \mathrm{i}(t_{+-} - t_{-+}) & (t_{++} - t_{--}) - \mathrm{i}(t_{+-} + t_{-+}) \\ (t_{++} - t_{--}) + \mathrm{i}(t_{+-} + t_{-+}) & (t_{++} + t_{--}) - \mathrm{i}(t_{+-} - t_{-+}) \end{bmatrix}. \tag{S14}$$

Section 5. Supplementary results of measurements

Figure S5 shows the measured intensity distributions of 2-channel PVs and 4-channel FVs, in the case that the LC orientation is along the *y*- and *z*- axis, at frequencies of f_0–f_2. Rather than working at a single frequency f_0, the intensity distributions exhibit the similar results for all the 12-mode vortices in an operating band of 80GHz within 0.44–0.52THz.

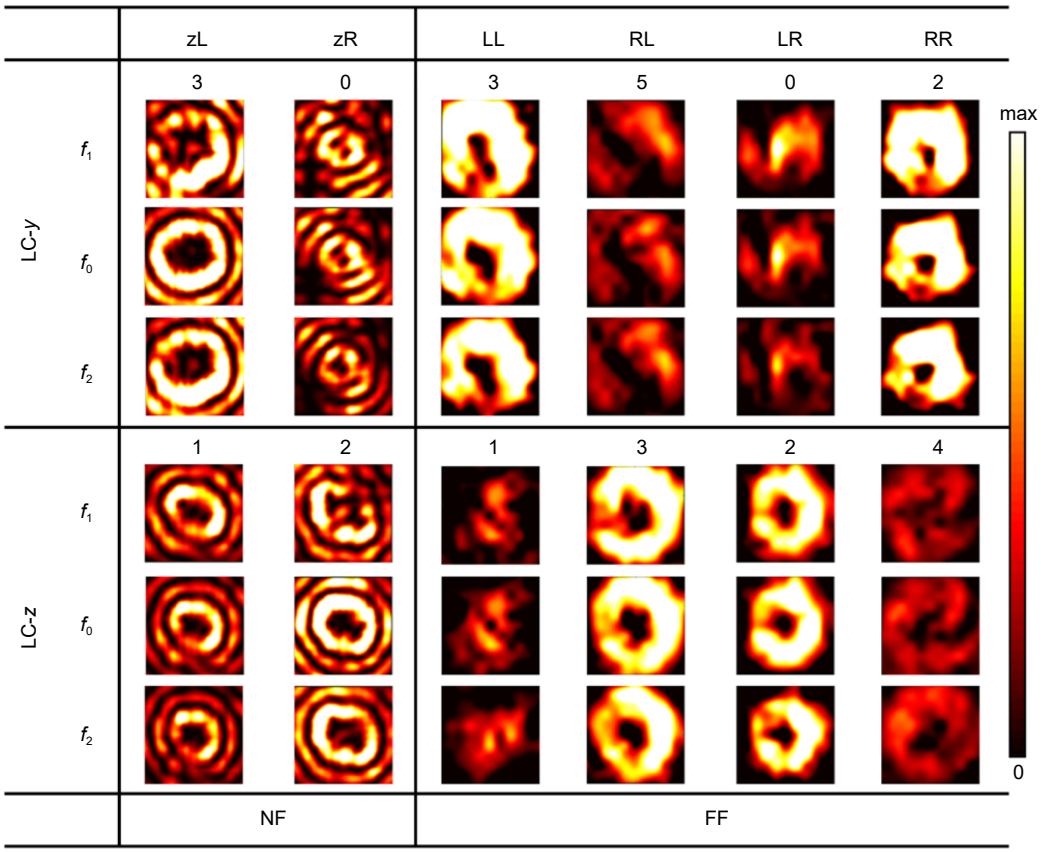

Fig. S5 | Measured intensity distribution of twelve mode vortices at f_0=0.475 THz, f_1=0.45 THz and f_2=0.5 THz.

The evolution of the simulated and experimental phase distribution shown in Fig. S6(a) and S6(b) are demonstrated as a support for the Fig. 6(a) in the main text, which illustrated that the topological charge numbers of FVs gradually changes from {3; 5; 0; 2} to {1; 3; 2; 4}.

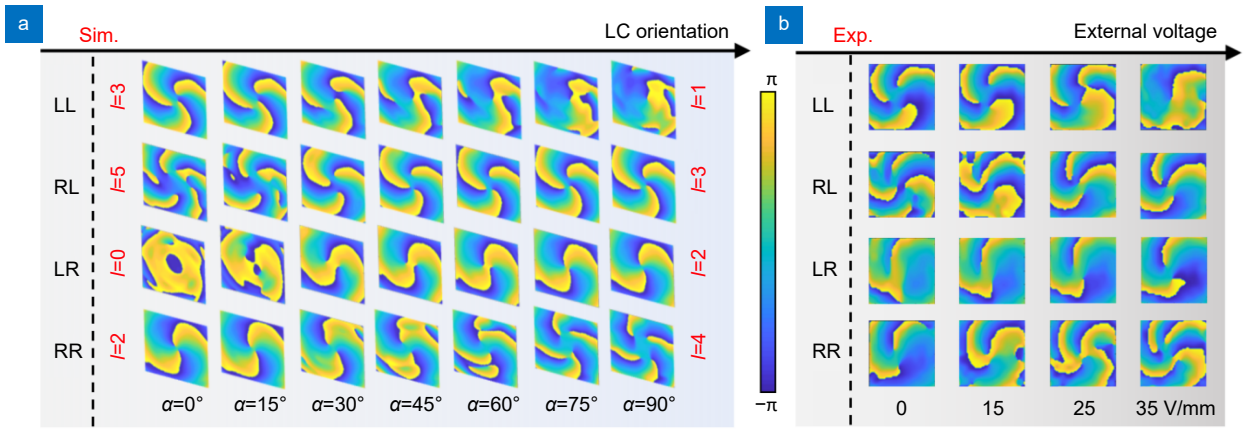

Fig. S6 | (**a**)The simulated and (**b**) measured dynamic conversion of phase distribution in 4 FF channels.

Section 6. Definitions and abbreviations

Abbreviations

FF	Far-feld
NF	Near-feld
PV	Plasmonic vortex
FV	Free-space vortex
SAM	Spin angular momentum
OAM	Orbital angular momentum
SPW	Surface plasmonic wave
LC	Liquid crystal
N/F-STS	Near/far-field scanning THz spectroscopy
LP	Linearly polarized
LCP	Left-circular-polarization
RCP	Right-circular-polarization

Definitions

1. Vortex types: including PVs (vortices in NF) and FVs (vortices in FF).
2. Vortex modes: a description containing both the photon states (SP state of z, or spin states of L and R) and the OAMs.
3. Vortex channels: associated with the spatial positions and the spin states, i.e. including NF channels of {zL; zR} and FF channels of {LL; RL; LR; RR}.
4. Parity conservation or parity breaking: describing the quantum numbers of OAM, that is, their topological charge numbers l.
5. Spin-decoupling or spin-locking: describing the vortex modes, of which the relationship between OAM and SAM.

References

S1. Yuan XY, Xu Q, Lang YH et al. Tailoring spatiotemporal dynamics of plasmonic vortices. *Opto-Electron Adv* **6**, 220133 (2023).